Pt_{147} nanoclusters soft-landed on WS_2 nanosheets for catalysis and energy harvesting

Biroju, Ravi K.; Harrison, Patrick; Theis, Wolfgang; Rees, Neil V.; Sharma, Rahul; Narayanan, Tharangattu N.; Hahm, Myung Gwan

DOI:
10.1021/acsanm.1c02683

Document Version
Peer reviewed version

Citation for published version (Harvard):
Biroju, RK, Harrison, P, Theis, W, Rees, NV, Sharma, R, Narayanan, TN & Hahm, MG 2021, 'Pt_{147} nanoclusters soft-landed on WS_2 nanosheets for catalysis and energy harvesting', *ACS Applied Nano Materials*, vol. 4, no. 12, 13140–13148. https://doi.org/10.1021/acsanm.1c02683

Pt_{147} Nanoclusters Soft-landed on WS_2 Nanosheets for Catalysis and Energy Harvesting

Journal:	*ACS Applied Nano Materials*
Manuscript ID	an-2021-02683y.R2
Manuscript Type:	Article
Date Submitted by the Author:	30-Nov-2021
Complete List of Authors:	Biroju, Ravi; University of Birmingham, School of Physics and Astronomy; Koneru Lakshmaiah Education Foundation, Department of Humanities and Sciences Harrison, Patrick; University of Birmingham, School of Physics and Astronomy Theis, Wolfgang; University of Birmingham, School of Physics and Astronomy Rees, Neil; University of Birmingham, Chemical Engineering Sharma, Rahul; Tata Institute of Fundamental Research Hyderabad, Material Sciences Narayanan, Tharangattu; Tata Institute of Fundamental Research Hyderabad, Centre for Interdisciplinary Sciences Hahm, Myung Gwan; Inha University, Department of Materials Science and Engineering

Pt_{147} Nanoclusters Soft-landed on WS_2 Nanosheets for Catalysis and Energy Harvesting

Ravi K. Biroju[§ab*], Patrick Harrison[§al], Wolfgang Theis[a], Neil V. Rees[c], Rahul Sharma[d], Tharangattu N. Narayanan[d] and Myung Gwan Hahm[e]

[a] Nanoscale Physics Research Laboratory, School of Physics and Astronomy, University of Birmingham B15 2TT, UK.

[b] Department of Basic Science and Humanities, Koneru Lakshmaiah Education Foundation Hyderabad 500075, Telangana, India.

[c] Centre for Hydrogen and Fuel Cell Research, School of Chemical Engineering, University of Birmingham, Birmingham, B15 2TT, UK.

[d] Surface Science and Interface Engineering Group, Tata Institute of Fundamental Research Hyderabad, Sy. No. 36/P, Serilingampally Mandal, Gopanpally Village, Hyderabad 500 107, India.

[e] Department of Materials Science and Engineering, Inha University, 100 Inha-ro, Michuhol-gu, Incheon, Republic of Korea 22212.

ABSTRACT

Understanding the interaction between metal nanoclusters and two dimensional (2D) layered materials presents a route towards the creation and tuning of hybrid materials. Here, we synthesize hybrid materials composed of mass-selected platinum nanoclusters produced using a magnetron sputtering gas aggregation cluster beam source with a lateral time-of-flight mass filter (mass resolution $M/\Delta M$ =20) and large-area tungsten disulfide (WS_2) 2D atomic layers. We employ aberration corrected scanning transmission electron microscopy (STEM) in high angle annular dark field (HAADF) mode and micro-Raman spectroscopy to study the interaction between Pt_{147} and

*Corresponding Author's E-mail: R.K.Biroju@bham.ac.uk or birojuravi@gmail.com

§Equally Contributing Authors

|Present Address: SIMAP Laboratory, CNRS-Grenoble INP, 1130 Rue de la Piscine, 38402 Saint Martin d'Hères, France

suspended WS_2 atomic layers. HAADF-STEM analysis reveals the soft landed Pt_{147} nanoclusters are situated on top of few layered WS_2 stacks, rather than being embedded or pinned. We observed a red shift in both E_{2g} and, A_{1g} modes and striking enhancement of A_{1g} mode in the micro-Raman signatures of WS_2, which provide evidence that Pt_{147} clusters are soft-landed on WS_2 basal plane without disrupting the crystalline structure of the WS_2 and of charge transfer from Pt_{147} to WS_2, respectively. In contrast, the measured change in line width of the E_{2g} mode of WS_2 reveals a strong interaction between Pt_{147} and WS_2 layers. Direct evidence for the relative stability of Pt_{147} clusters on WS_2 is assessed by position dependent Raman profiling and real-time HAADF-STEM imaging. Our approach offers a novel route to the controlled incorporation of size-selected nanoclusters on 2D WS_2 basal plane for catalysis and energy harvesting device applications.

Keywords: *2D materials, WS_2 atomic layers, Physical Vapour Transport, mass-selected Pt nanoclusters, gas phase cluster-beam deposition, High Angle Annular Dark Field (HAADF)-Scanning Transmission Electron Microscopy (STEM), Stacking Sequence*

1. INTRODUCTION

The deposition of size-selected nanoclusters onto surfaces offers a route to explore fundamental cluster–surface interactions,[1] as well as the possibility to develop novel materials for diverse applications in interdisciplinary science[2]. Well defined nanoparticles (NPs) or clusters deposited onto two-dimensional (2D) layered materials such as graphene and transition metal dichalcogenides (TMDs: MoS_2, WS_2 etc.) represent a class of materials with controllable properties that can be tuned by embedding the nanoparticles or through the creation of surface defects.[3-4] Some recent examples include the deposition of size-selected Pd_n ($n \leq 20$) clusters on supported graphene[3], the propagation of Au_n ($n = 55, 923$) nanoclusters through few-layered graphene[5] and the observed preferential nucleation of Pt clusters at grain boundaries of polycrystalline MoS_2.[6] Studying the differing behaviours between single atoms or small few-atom clusters and NPs on 2D surfaces is crucial to understanding the

pathways of clusters nucleation and growth.[1] Owing to quantum confinement effects, clusters exhibit a range of size-dependent physicochemical properties that can be investigated experimentally by employing size-selection to achieve narrow size dispersions. Cluster beam deposition (CBD) offers control over the deposition of ligand-free nanoparticles onto surfaces[7], not only in terms of particle size, but also surface coverage and surface impact energy and thus provides a root to create well-defined nanostructured surfaces consisting of monodisperse nanoparticles.[7]

Graphite is a conventional model substrate that has been used to study properties of size-selected clusters.[5] Three deposition regimes have been identified for clusters on graphite, namely, soft landing, pinning and implantation. Soft landing requires that cluster atomic kinetic energies per atom are sufficiently smaller than atomic binding energies (few eV) to avoid fragmentation on impact, however soft-landed clusters are typically free to diffuse and aggregate at room temperature.[1] At higher impact energies the clusters may become pinned due to the creation of surface defects on impact or implanted through many layers[8]. The knowledge gained from such studies on graphitic surfaces[3] provides a path to study this interaction with other 2D layered materials such as MoS_2 and WS_2.[6, 9-10]

The interaction between metals and 2D materials is currently of great interest due to the development of 2D layered materials along with metal composite materials[10-12] and the influence of these metals on the hybrid electronic and catalytic properties of 2D materials.[13] Recent electron microscopy studies have focussed on the behaviour of metals, in particular Au deposited onto graphene by physical methods[13-14] and Pt on MoS_2 by physical[6, 9, 15] and wet[11] methods. An in-situ atomic scale study reported on the formation of epitaxial Pt nanocrystals on monolayer MoS_2[9] that possess promising catalytic properties for hydrogen evolution (HER).[15-16] The authors found two types of preferential alignment between the Pt nanocrystals and the underlying monolayer MoS_2. In this view, WS_2 and Pt-WS_2 hybrid materials can show promising visible light photocatalytic properties for HER and understanding their detailed structures at the atomic scale is crucial to further development[17]. To the authors knowledge, there are no reports on HAADF-STEM studies of size-selected metal nanoclusters on 2D TMD materials platform using cluster beam deposition (CBD).

Fabrication of size-selected Pt clusters on WS_2 2D support using a novel route of fabrication via CBD will pave a way to explore new avenues in catalysis applications. On the other hand, platinum nanoparticles are well researched due to their importance as catalysts, including within the field of alternative energies[18]. Under electrochemical conditions within polymer exchange membrane fuel cells, it has been shown that platinum may degrade by different mechanisms, including sintering and coalescence[19], Ostwald ripening[20], or dissolution into the reaction medium[21]. Understanding both the role of the catalyst within the reaction, but also the different catalyst degradation pathways is critical to improving performance and efficiency[22]. To this end recently, size-selected nanoclusters have been used as model systems to study nanoparticle-surface interactions[23], degradation[24], and intrinsic nanoparticle properties due to their well-defined sizes[25] and shapes[26]. Wettergren et al.[25] demonstrated that monodispersed size-selected platinum nanoclusters show high sintering resistance under reaction conditions compared to bidispersed samples containing the same sized clusters.

The structures of platinum nanoclusters have been studied theoretically[27-28] and experimentally[27,29]. At sizes below n<300 atoms Lambie et al.[27] observed that the structures of size-selected Pt_n nanoclusters were predominantly amorphous whilst noting structural 'ring-dot' features common to icosahedral motifs, whereas at larger sizes the nanoclusters had increasingly common bulk phase face-center cubic (FCC) structures. Octahedral (FCC) platinum clusters were also observed by Xia et al.[29] for large sizes (n>5000). Clusters with closed-shell structures represent the so-called 'magic number' clusters and are predicted to have increased stabilities[30]. For cuboctahedral, decahedral, and icosahedral motifs these magic number structures occur at common sizes, namely n=55, 147, 309, 561 etc., and have been observed in small noble metal clusters[27, 31-34]

In the present work, we demonstrate the use of CBD to produce well-defined catalytically relevant hybrid nanostructured 2D materials. Size-selected Pt_{147} clusters were

deposited in the soft-landing regime on physical vapour transport (PVT) grown WS_2 atomic layers. The arrangement of Pt_{147} clusters on the suspended WS_2 atomic stacks was quantified through HAADF-STEM imaging, demonstrating that no significant aggregation or coalescence of Pt_{147} on the WS_2 layers occurred. Furthermore, the E_{2g} and A_{1g} Raman signatures of suspended WS_2-Pt_{147} clearly reveal doping and strain enhancement attributed to the strong interaction of Pt_{147} clusters with the WS_2 basal plane. Our results represent new findings on the hybrid materials based on atomic-layered WS_2 using gas phase CBD technique and bear importance towards the development of atomic- layer-based hybrid photocatalysts.

2. EXPERIMENTAL

2.1. Physical vapour transport growth of WS_2 atomic layers

Tungsten disulfide (WS_2) atomic layers were grown over 300 nm thick SiO_2/Si via PVT technique. A two-zone furnace was used with a separate heater for both chalcogenide and metal oxide WO_3 source. The whole PVT process was confined within a cylindrical quartz tube of an inner diameter 45 mm as shown in the Figure 1(a). The WS_2 precursors were loaded into two alumina boats inside a quartz tube chamber. The central boat was filled with 70 mg of WO_3 and 15 mg of NaCl and the second boat maintained at the low temperature end of the furnace was filled with 500 mg sulfur (S). Note that the SiO_2/Si substrates were kept on top of the central boat. Initially the tube was first evacuated to 10^{-3} mbar and then filled with Ar/H_2 mixture gas up to atmospheric pressure. A uniform flow of 400 sccm Ar/H_2 was maintained through the tube. Sulfur was evaporated at 180 ºC whilst the central zone of the tube was heated up to ~825 ºC. The system was operated to allow WS_2 to grow for 20 minutes before inhibition through sudden cooling of the system.

2.2. Wet transfer of WS_2 atomic layers

Prior to the deposition of Pt_{147} clusters on WS_2 atomic layers, PVT grown WS_2 was transferred on to TEM quantifoil grids by a wet transfer method (copper quantifoil TEM grids covered with a holy

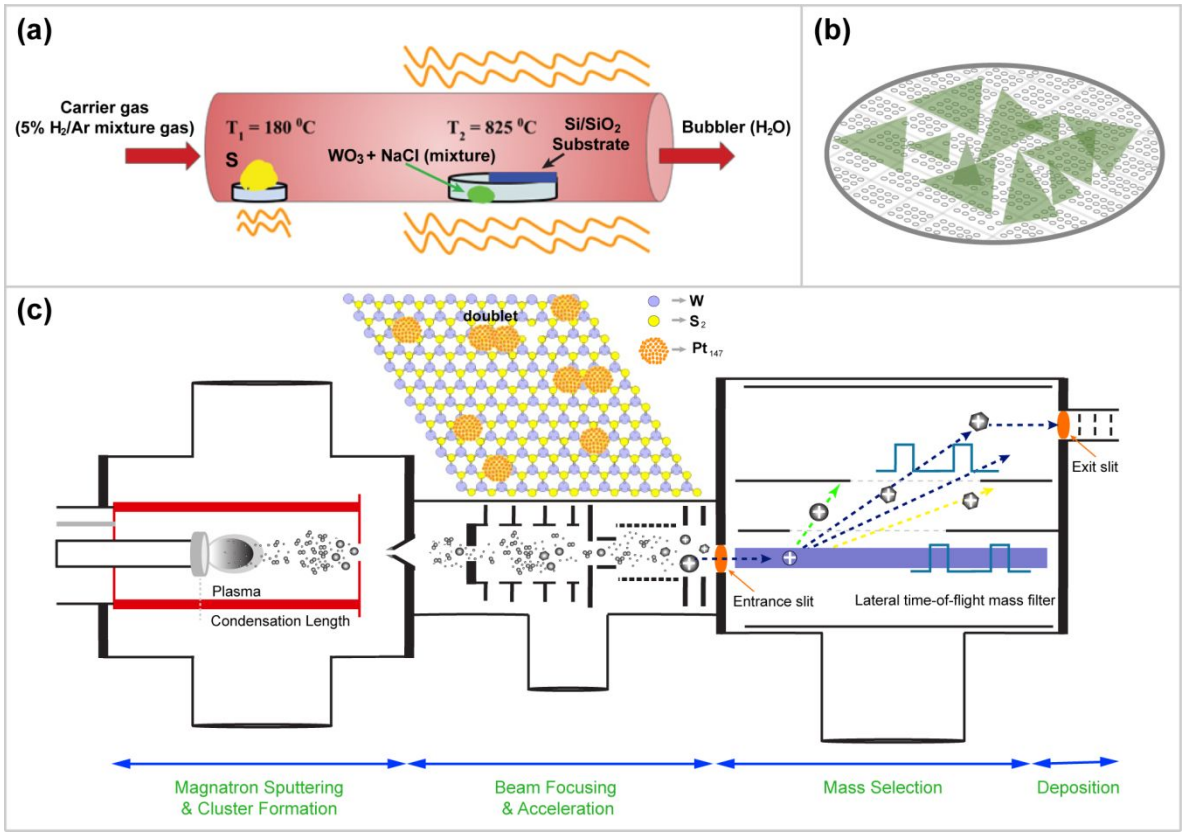

Figure 1: Schematic illustration of the fabrication of WS_2-Pt_{147} hybrid nanostructured 2D materials. Schematic of the (a) PVT growth of WS_2 nanosheets, (b) wet-transferred WS_2 nanosheets on a Cu quantifoil TEM grid, and (c) the cluster source, which contains four main regions: cluster formation, beam focussing, mass selection, and cluster deposition. Note that the inset of figure (c) denotes the schematic model of the WS_2-Pt_{147} hybrid material.

carbon layer with holes of 2µm diameter (QR1213400Cu25, Quantifoil R1.2/1.3 400 mesh copper grids, EM Resolutions, UK)) as shown in the schematic Figure 1(b). Note that the complete experimental details of the wet transfer method of WS_2 are found in the supporting information, Figure S1. In this method, a thin poly(methylmethacrylate) (PMMA) layer was coated onto the $WS_2/SiO_2/Si$ substrate and cured at 180 ˚C for 10 minutes. The samples were then dried at room temperature for several hours. $PMMA/WS_2/SiO_2/Si$ substrates were then floated on 5% HF etchant solution overnight to separate the $PMMA/WS_2$ and subsequently transferred onto TEM quantifoil grids. Note that care was taken while scooping the PMMA supported WS_2 layers onto the substrate as the layers are easily broken and may become contaminated. The substrate containing WS_2 was then

heated on a hot plate up to 180 ºC to adhere to the sample properly for drying. Finally, the PMMA layer was etched using acetone several times. The sample was rinsed in isopropyl alcohol (IPA) for a couple of minutes and dried before HAADF-STEM imaging.

2.3. Cluster beam deposition of size selected Pt_{147} clusters on WS_2 sheets

Size-selected platinum clusters were generated using a DC magnetron sputtering and gas condensation cluster beam source[34-36] as shown in the schematic Figure 1(c). Briefly, clusters are condensed in the gas phase after Ar plasma sputtering from a 2-inch sputtering Pt target (PI-KEM, 99.99% purity). The positively charged clusters are accelerated with electrostatic lenses to form a cluster beam, which is filtered prior to deposition onto a substrate under high vacuum conditions (10^{-7} mbar) using an inline lateral time-of-flight mass selector[37] with a nominal mass resolution of $M/\Delta M$ = 20. A mass spectrum demonstrating the resolution of the cluster source used in this study is shown in the supporting information, Figure S2. A mass of 28665 amu, corresponding to 147 Pt atoms (designated as Pt_{147}), was selected for deposition on to suspended WS_2 atomic layers supported on mesh type holey carbon coated TEM grids. Note that the TEM grid was loaded into the deposition chamber such that the WS_2 atomic layers were directed at the impinging cluster beam. The deposition (impact) energy of the clusters was controlled by a bias voltage applied to the substrate. Here, the deposition energy was maintained at 1eV per atom, ie. typical soft landing conditions as the atomic binding energy has been calculated to be ~ 4.5 eV per atom for Pt_{147}[8]. The cluster beam current incident on the sample was monitored during deposition, and the total dose was determined by integrating over the deposition time. Previous studies of size-selected Pt clusters with up to 2000 atoms soft-landed at 1eV per atom onto amorphous carbon film TEM grids have shown that the clusters maintained a spherical geometry on the substrate (results are not shown here).

2.4. High-angle annular dark-field scanning transmission electron microscopy (HAADF-STEM)

Scanning transmission electron microscopy (STEM) was performed using a JEOL 2100F microscope with spherical aberration-correction (CEOS GmBH) and an accelerating voltage of 200 kV. The microscope was operated in high-angle annular dark-field (HAADF) mode to achieve Z-contrast imaging where the inner and outer collection angles of the annular detector were 62 and 164 mrad, respectively. The probe semi-convergence angle was 19 mrad.[38-39] Each HAADF-STEM image was obtained in a frame of 512 × 512 pixels with a dwell time of 38 μs per pixel.

2.5 Raman Measurements

Micro Raman measurements were performed with a high-resolution spectrometer (Renishaw Invia, UK), with excitation wavelength (λex) of 532 nm (Diode laser). The excitation source was focused with a 100× objective lens, a spot size of 2 μm, and a laser power of 1 mW to avoid heating and damage to the sample, and the signal was collected by a CCD camera in a back scattering geometry sent through a multimode fiber grating with 2400 grooves/mm. Note that the Raman analysis shown here for the suspended WS_2 and suspended WS_2-Pt_{147} samples on TEM quantifoil grids were recorded for an exposure time of 1 second.

3. RESULTS AND DISCUSSION

3.1. HAADF-STEM studies:

In order to demonstrate the areal distribution of Pt_{147} on a few-layered WS_2, the as-transferred WS_2 atomic layers were first characterized with HAADF-STEM. Figure 2 shows the crystalline structure and homogeneity of the prepared WS_2 sheets. The contrast in the HAADF image is sensitive to both the atomic number and number of atoms under the electron beam[40-41], thus providing information to identify the number of layers and detailed atomic arrangement.[42] Figure 2(a) shows the low-resolution HAADF-STEM image of few- layered WS_2 multilayer stacks after wet transfer onto a STEM quantifoil grid. Figure 2(b) shows the HAADF-STEM image of a step edge between mono- and bi-layered WS_2 in the field of view. The few-layer flake is stacked with concentric triangular, and polygon shaped atomic layers, leading to the observable contrast from step edges as shown in Figure

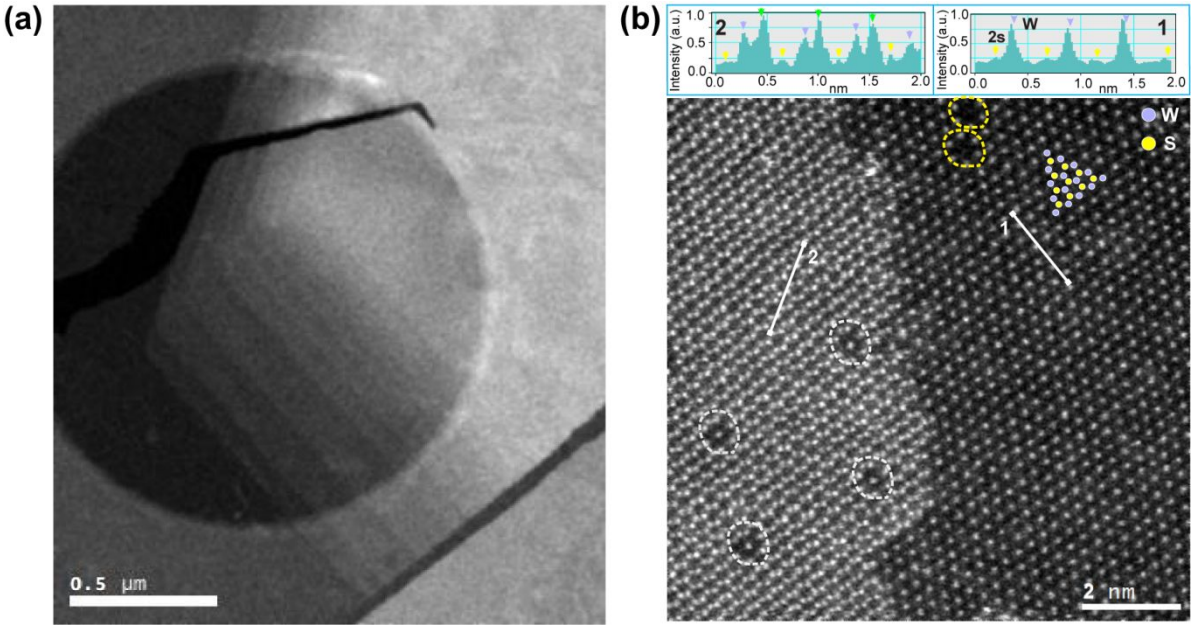

Figure 2: Atomic resolution HAADF-STEM imaging of suspended WS_2 atomic layers. (a) Low resolution HAADF-STEM image of WS_2 stacks, and (b) HAADF atomic resolution image of a bi-layered WS_2. Yellow and white dashed circles indicate single and multi-vacancies of W atoms present on the full and partial monolayer, respectively. Note that the top insets are the intensity profiles corresponding to mono and bilayer regions represented by lines 1 and 2, respectively. The bright spots correspond to 'W' atoms, while columns are filled with 'S' atoms.

2(a). The bilayer region (left) has higher average HAADF intensity in the image, and the median HAADF intensity is found to be directly proportional to the number of WS_2 atomic layers (see supporting information, Figure S3). Note that the top insets in Figure 2(b) correspond to the HAADF intensity line profiles of W (Blue arrow) and S (yellow arrow) across mono- and bi-layered WS_2, which are extracted from regions 1 and 2 in the HAADF image, respectively. The yellow and white dashed circles in Figure 2(b) denote the single and multi-vacancy defects due to missing W atoms within the mono- and bi-layered WS_2, respectively. These might be intrinsic defects formed during PVT growth of WS_2 that are unavoidable or partially due to electron beam irradiation[43], an example of the observed damage to monolayer WS_2 by the electron beam during STEM imaging is shown in the supporting information, Figure S4. The two most common low energy arrangements of W and S atomic columns in bi-layered WS_2 during PVT growth are the 2H (AA') and the 3R (AB) types,

where 2H stacking is produced by a 60° rotation of one layer with respect to the other, and the atomic columns contain one metal and two chalcogenide atoms when viewed along with the layer normal, which gives the same contrast for each column in an HAADF-STEM image[43]. Note that the bright dots correspond to W atoms while columns among them are filled with top and bottom S atoms (see Figure 2(b)). A schematic of the molecular model of a bilayer WS_2 with both stacking arrangements is shown in the supporting information, Figure S5. For the AB (3R) stacked bilayer, both layers have the same lattice orientation but are offset (see Figure 2(b)). Each atomic column then falls into one of three categories: W + 2S, W, or 2S, which in turn gives three contrast signals in an HAADF-STEM image[43], and are denoted by green, blue, and yellow arrows in Figure 2(b) inset, respectively. Two important observations were noticed, firstly that the relative HAADF intensity of S atoms are approximately one order smaller (if Rutherford alpha coefficient = 2) compared to W atoms in a single layer, and secondly that there is a difference in HAADF intensity between neighbouring columns due to the presence (or not) of underlying S in case of bi-layered WS_2. Columns containing single S atoms have very low HAADF intensity in the atomic resolution HAADF images of the WS_2 atomic layer, as shown in the line profiles in Figure 2(b). These two observations are in good agreement with our experimental HAADF-STEM imaging with previously reported works[43-44]. Thus, figure 2(b) confirms that the dominant phase of the bi- and few-layered WS_2 was found to be 3R for these samples, which were used for the WS_2-Pt_{147} hybrid. In addition, we have performed XPS measurements on pristine WS_2 as shown in the supporting information, SI1, Figure S6, which confirm the chemical composition of 3R phase WS_2 nanosheets.

A detailed HAADF-STEM analysis of WS_2-Pt_{147} hybrid nanostructured 2D material is demonstrated in Figure 3. Figure 3(a) presents a HAADF image of size selected Pt_{147} clusters deposited with 1eV per atom kinetic energy onto WS_2 atomic layers. Several HAADF-STEM images of the synthesized WS_2-Pt_{147} hybrid are shown in the supporting information, Figure S7. HAADF intensity analysis was used to 'weigh' the number of layers in a few layered WS_2. Figure 3(b) shows a HAADF-STEM image of few-layered WS_2 extracted around line profile 6 in Figure 3(a) and its corresponding HAADF intensity. Assuming the bilayer contributes two monolayer intensities, four-

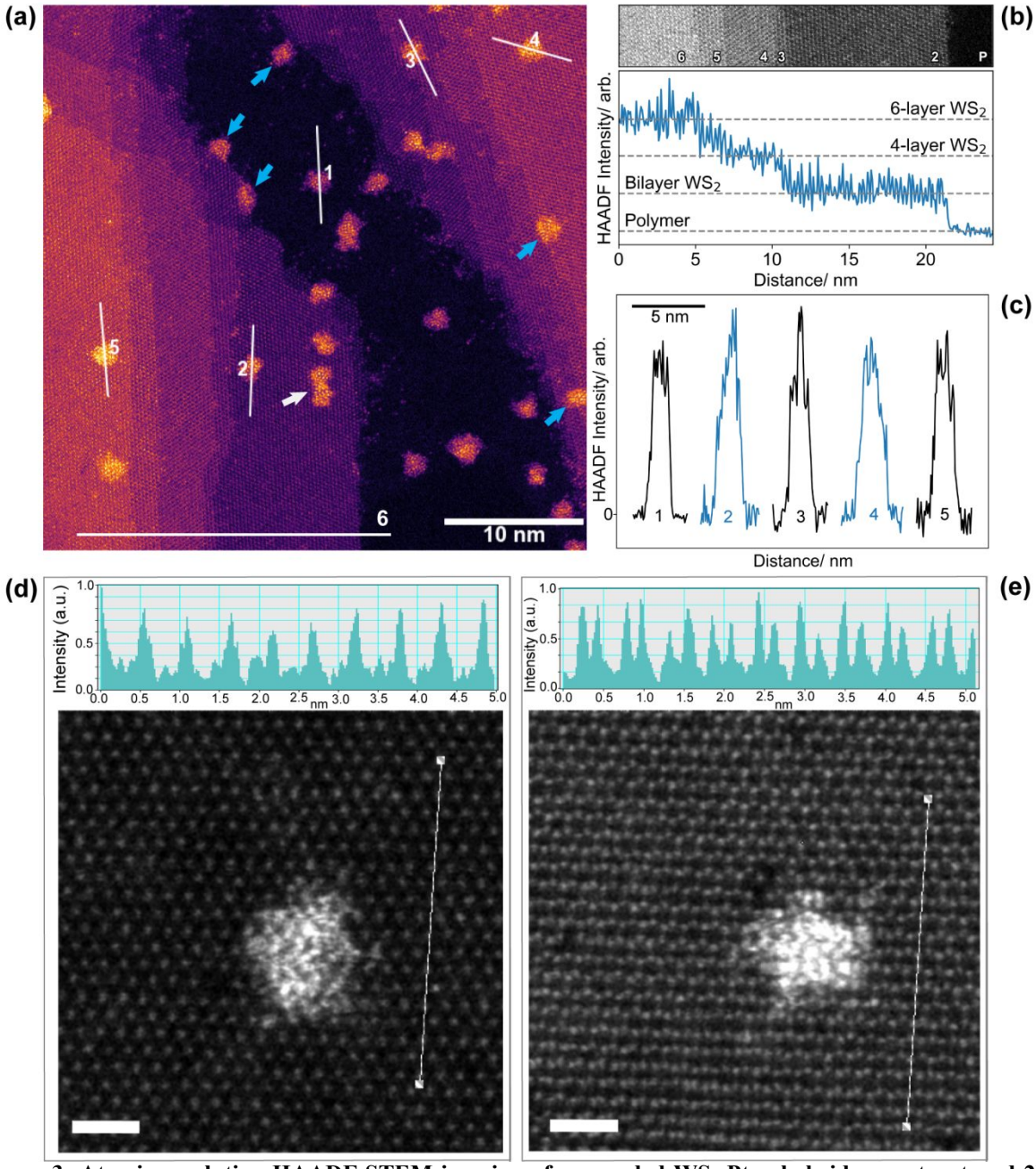

Figure 3: Atomic resolution HAADF-STEM imaging of suspended WS_2-Pt_{147} hybrid nanostructured 2D materials. (a) HAADF-STEM image of Pt_{147} deposited with 1 eV per atom kinetic energy onto few layered WS_2. Note that the image is processed using image J software and a fire false colour lookup table (LUT) was applied to improve the visual perception. (b) HAADF-STEM image and corresponding line profile intensity are extracted from line profile 6 in (a). The median HAADF intensities of 4- and 6-layer WS_2 are 2.00±0.16 and 2.97±0.21 times the average bi-layered WS_2 HAADF intensity. (c) Local background subtracted intensity profiles of Pt_{147} clusters across the polymer (1), bilayer (2), tri layer (3) and few-layer (4-6) WS_2 substrate, which are extracted from the marked regions of figure (a). (d-e) HAADF Image of the single Pt_{147} on mono- and bi-layered WS_2. Corresponding HAADF intensity profiles (top inset) of the

mono- and bi-layered WS_2 in 3R stacking are shown in the top insets. Note that the scale bar denoted in (d-e) is 1 nm.

and six-layer WS_2 have the intensity corresponding to 3.98 and 5.94 monolayers, respectively. The agreement of these values indicates that the prepared WS_2 layers are situated on top of a layer of residual polymer from the fabrication process, which is confirmed through Bright-Field STEM imaging as shown in Figure S8. Figure 3(c) depicts the intensity profiles of the indicated clusters showing that the cluster intensity is consistent across the different backgrounds, such as the polymer (P), bi-layer (2), few-layer (3-6) backgrounds indicating that the soft-landed clusters sit on the top of the WS_2 sheets rather than being embedded in them. Pt_{147} clusters can also be found on both mono- and few-layered WS_2 at both step edges and on the basal plane. Note that the cyan arrows in Figure 3(a) indicate the Pt_{147} clusters situated at the step edges of mono to few-layered WS_2 while a white arrow indicates the two sintered Pt_{147} clusters. Figure 3(d-e) depict high resolution HAADF images of single Pt_{147} nanoclusters soft landed onto monolayer and 3R stacked bi-layer WS_2, respectively. The corresponding intensity profiles marked in Figure 3(d-e) are shown in the top insets. Interestingly, a slight misorientation of the bi-layer WS_2 can be seen at the bottom of the Figure 3(e) leading to the contrast difference in the line profiles of W+2s, W and 2S columns, respectively. However, studying atomic reconstruction in twisted bilayers of 2D TMDs is a fascinating topic in the current research on 2D materials, which possess interesting physicochemical properties for future perspectives.[45]

Figure 4(a) represents the size distribution of Pt clusters deposited onto WS_2 atomic layers as calculated by their integrated HAADF intensity. Two peaks are observed in the distribution corresponding to the size of deposited Pt_{147} singlets (red fit) and a secondary peak at larger sizes. The inset in Figure 4(a) shows that the integrated HAADF intensity of the second peak is two times larger than the primary peak, indicating that the second peak is constituted from the integrated intensities of two sintered Pt_{147} clusters. The Pt_{147} clusters have a radius of 0.79±0.04 nm as shown in the radial size distribution in the supporting information, Figure S9, this is in good agreement with the theoretical radius for spherical Pt_{147} calculated at bulk density. This is further evidence that Pt_{147} retain

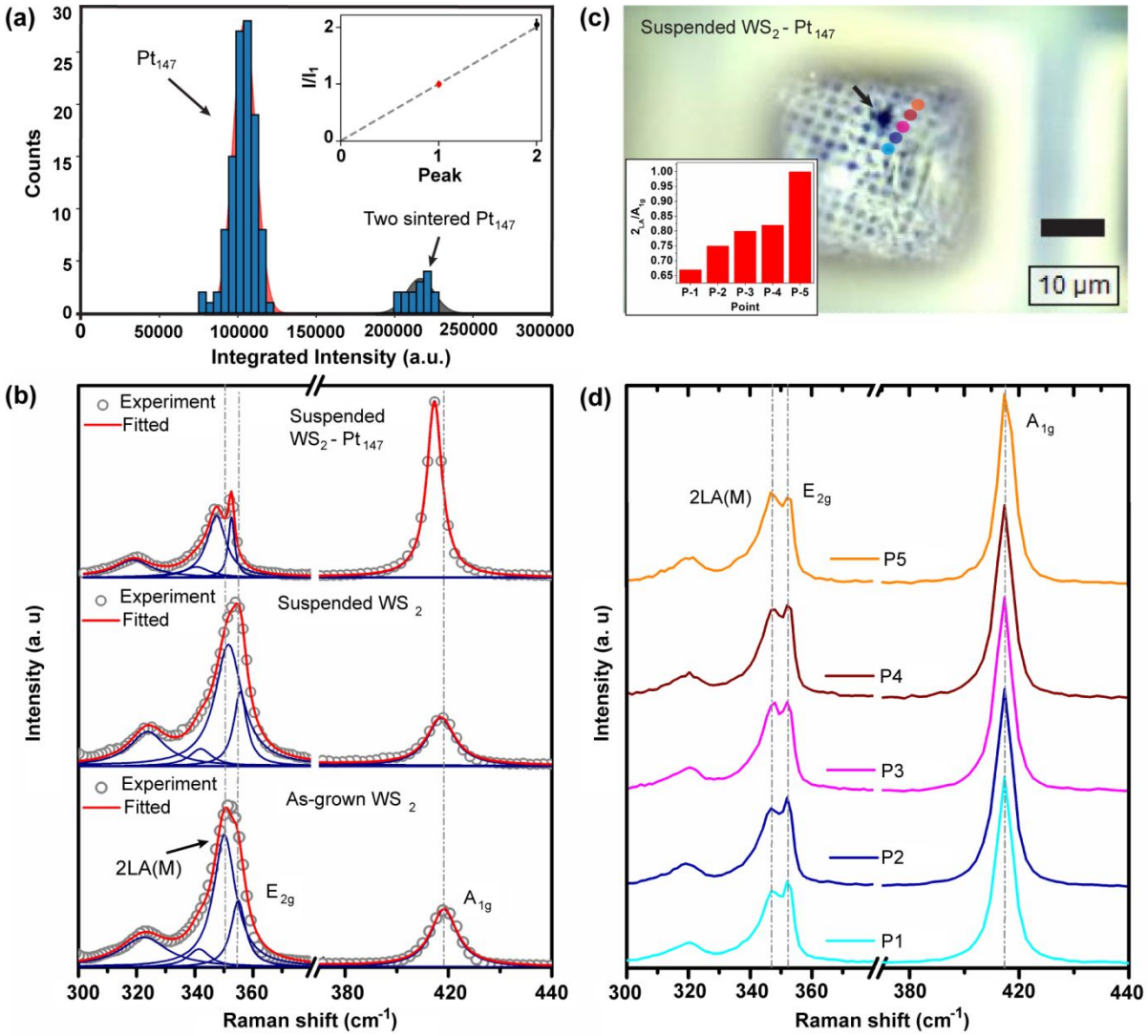

Figure 4: (a) Integrated HAADF intensity distribution of Pt_{147} deposited with 1 eV per atom onto WS_2 nanosheets. Inset shows the integrated intensity ratio of the two distributions confirming that the secondary peak is constituted from two sintered Pt_{147} clusters. (b) Raman signatures of suspended WS_2-Pt_{147}, suspended WS_2 and as-grown WS_2 on Si/SiO_2 substrate. Note that the dotted lines denote the experimental data whereas the solid line corresponds to fitted data. (c) Optical microscope image of suspended WS_2-Pt_{147} recorded with 100x objective lens. Inset of (c) is the calculated $2_{LA(M)}/A_{1g}$ ratio as a function of scanning position. (d) Point Raman spectra recorded at the corresponding locations shown in (c).

spherical geometries on top of each substrate and that there is no significant cluster wetting. The dominant primary peak in both distributions provides evidence that Pt_{147} do not undergo significant diffusion and aggregation on WS_2 at 1eV per atom deposition energy. The projected area distribution

of the Pt_{147} clusters is broader (ie. width divided by mean value) than the integrated intensity distribution due to various reasons, including thresholding uncertainties and differing Pt_{147} arrangements and structures on the WS_2 surface. For these reasons integrated HAADF intensity is more robust descriptor for small metal clusters[46]. High resolution imaging of the Pt_{147} clusters on WS_2 as shown in Figure S10 reveals predominantly non-crystalline structures, with structural features indicative of partial icosahedral motifs, which is consistent with the findings of Lambie et al.[27]. Larger sintered clusters, identified through their integrated HAADF intensity, are observed to have crystalline FCC structures.

3.2. Raman studies: Physical characterization of WS_2 and WS_2-Pt_{147} clusters

In-order to probe the interaction of Pt_{147} size-selected clusters with WS_2, we performed Raman spectroscopy measurements on suspended WS_2 and suspended WS_2-Pt_{147}. Figure 4(b) shows the Raman fingerprints acquired from as-grown WS_2 on SiO_2, and suspended WS_2 before and after Pt_{147} deposition. Note that the optical microscope (OM) images and corresponding photoluminescence mapping of as-grown WS_2 on SiO_2 are shown in the supporting information, Figure S11. Figure 4 (c-d) show the position dependent Raman profiles of a suspended WS_2-Pt_{147} acquired at several locations on the quantifoil TEM grid. Note that the arrow indicates sample damage due to prolonged laser exposure (>1 second). The characteristic Raman features in most of the TMDs including WS_2 are E_{2g} and A_{1g} modes, E_{2g} originates from the in-plane vibration of two 'S' atoms with respect to the 'W' atoms, whereas the A_{1g} mode is associated with the out-of-plane vibration of only 'S' atoms in opposite directions with respect to the 'W' atoms.[47-51] The Raman signal of WS_2 at 532 nm laser excitation produced a very strong response, which contains not only E_{2g} and A_{1g} but also many second order Raman modes, including 2LA(M)[47-48]. The $E_{2g}(\Gamma)$ and $2_{LA(M)}$ modes overlap but were resolved using Lorentzian fitting. The Raman signal was fitted in total with five Lorentzian peaks, centred at ~ 322 cm^{-1}, 341 cm^{-1}, 350 cm^{-1} (Longitudinal modes (LA)), 354 $cm^{-1}(E_{2g})$, and 419 $cm^{-1}(A_{1g})$ in case of as-grown WS_2 on SiO_2 in comparison with the suspended WS_2 and suspended WS_2-Pt_{147} samples as shown in Figure 4(b). Note that the complete details of the Lorentzian fitting analysis are shown in the

supporting information, Table-3, and Table-4. Among all of the observed modes, 2LA(M), E_{2g}, and A_{1g} have been extensively studied and proven to the local environment and induced strain[47]. The Raman features of as-grown WS_2 on SiO_2 and suspended WS_2 are almost identical with respect to their peak positions. However, the integrated intensity ratio $I_{2LA(M)}/I_{A1g}$ for monolayer WS_2 should be more than ~ 2.5[47]. In the present case the, $I_{2LA(M)}/I_{A1g}$ ratio is found to be 3.33 in the case of as-grown WS_2, which is further enhanced to 4.37 for suspended WS_2, demonstrating the high quality of these WS_2 monolayers. Interestingly, $I_{2LA(M)}/I_{A1g}$ was significantly reduced to 0.77 for suspended WS_2-Pt_{147}, which may be due to the coverage of Pt_{147} clusters over these WS_2 layers.[48] The Raman characteristics of suspended WS_2-Pt_{147} layers are completely different from suspended and as-grown WS_2. The E_{2g} peak in the suspended WS_2-Pt_{147} sample shows a 2 cm^{-1} red shift when compared to suspended WS_2 which may be due to strain enhancement in the suspended WS_2 lattice in the presence of Pt_{147} clusters[47].

Furthermore, the position dependent $I_{2LA(M)}/I_{A1g}$ ratio (see Figure 4(d)) is found to be marginally increasing at different points of suspended WS_2-Pt_{147} as shown in the histogram plotted for each point at corresponding scanning location (see inset of Figure 4(c)). Two important observations are taken from this position dependent Raman profiling, one may be the change in the morphology of Pt_{147} clusters and other may be increase in the local environment of density of defects and induced strain on the WS_2 basal plane due to the presence of Pt_{147} at neighbouring scan locations between points 1 and 5. Further, the strain enhancement in suspended WS_2-Pt_{147} is estimated from the $I_{2LA(M)}/I_{A1g}$ ratio in the position dependent Raman analysis, which is found to have increased by a factor of 1.3 in the case of suspended WS_2, and decreased by a factor of 4.3 in the case of suspended WS_2-Pt_{147} with respect to as-grown WS_2 on SiO_2, respectively. The $I_{2LA(M)}/I_{A1g}$ ratio of WS_2-Pt_{147} is reduced to 74% with respect to the as-grown WS_2. This is consistent with real-time HAADF-STEM data of suspended WS_2-Pt_{147} under the electron beam, which will be discussed later. On the other hand, the A_{1g} peak of suspended WS_2-Pt_{147} also shows a 2 cm^{-1} red shift which may be a consequence of charge transfer from Pt_{147} clusters to WS_2 as A_{1g} is reportedly sensitive to the doping and substrate effect[46] and shows a redshift when there is an increase in electron concentration[47]. Thus, the collective

Raman features not only confirm the presence of Pt_{147} clusters but also show a charge transfer effect from Pt clusters to WS_2 layers. The effect of charge transfer and strong interaction between WS_2-Pt_{147} was confirmed from photoluminescence (PL) studies of pristine suspended WS_2 and suspended WS_2-Pt_{147} as shown in the supporting information, Figure S12 for these samples. In principle the PL emission centred at 630 nm corresponds to monolayer WS_2[49]. Interestingly, we noticed a red shift (642 nm) after the deposition of Pt clusters on the WS_2 atomic layers. The observed red shift (12 nm) from suspended WS_2-Pt_{147} may be due to the rise in the Fermi level of WS_2, which denotes significant charge transfer from Pt to WS_2[49, 53-54]. This PL evolution in suspended WS_2-Pt_{147} is in good agreement with the Raman shift observed, particularly for the A_{1g} peak of WS_2.

The relative stability of Pt_{147} clusters under the electron beam on mono- to few- layered WS_2 is further substantiated by real-time HAADF-STEM imaging of Pt_{147} clusters on the WS_2 basal plane as shown in the supporting information, Figure S13. Real-time HAADF-STEM imaging was performed by consecutively acquiring 50 HAADF image frames, which were recorded with an interval of 30 seconds for each frame at the same location. Note that the constructed movie, which is shown in Figure S14, is a collection of all these real HAADF images acquired at the same location of the free-standing monolayer WS_2-Pt_{147} sample. The distance between the two clusters at the centre of the frame is calculated for frames 1, 25 and 50 as shown in Figure S13 and is found to reduce for longer beam exposure due to an increase the number of defects in WS_2 created by its interaction with the imaging electron beam. Interestingly, the cluster was also observed to change from a spherical to dumbbell morphology without migration over the WS_2 surface, suggesting a strong substrate interaction. Real time HAADF-STEM imaging revealed that the clusters are relatively stable with respect to electron beam exposure and do not agglomerate on the surface, which is in good agreement with position dependent Raman line shape analysis discussed previously.

4. CONCLUSION

To summarize, we have studied the morphology of ultra-small, mass-selected Pt_{147} clusters soft-landed at 1 eV per atom kinetic energy onto large- area 2D WS_2 atomic layers by cluster beam

deposition. We find that Pt_{147} clusters are relatively stable on mono- to few- layered WS_2 *i.e* they are not free-moving and do not agglomerate on the surface. Raman studies in conjunction with HAADF-STEM imaging provide direct evidence that soft-landed Pt_{147} clusters remain stable and isolated on WS_2. Based on the clear redshift in both E_{2g} and A_{1g} signatures of WS_2, there is a significant WS_2-Pt_{147} interaction, and the observed enhancement of A_{1g} mode shows charge transfer from Pt_{147} to WS_2. Our studies highlight the utility of size selected nanoclusters on mono- to few-layer WS_2 supports for the development of 2D WS_2 based functional materials for catalysis applications.

ACKNOWLEDGEMENT

This work was supported financially by the HORIZON 2020, H2020 Marie-Skłodowska-Curie Actions (Grant Numbers: H2020-MSCA-IF-2017, 750929). Dr. Ravi K. Biroju acknowledges Prof. Richard E Palmer, Swansea University, and Dr. Shane Murphy, Technological University Dublin for their support. This work was supported by a National Research Foundation of Korea (NRF) grant funded by the Korean government (MSIT, Ministry of Science and ICT) (Grant No. NRF-2020R1A2C2009378). We gratefully acknowledge Catherine Storey, Experimental officer, NPRL, for her assistance in some part of the sample preparation. We acknowledge Dr. Balakrishna Ananthoju and Prof. Robert A W Dryfe for doing XPS measurements. We thank to Dr. Ziyou Li, NPRL, for helping with HAADF-STEM image analysis of WS_2-Pt_{147} hybrids. Dr. Ravi K. Biroju would like to dedicate this paper to Dr. Ziyou Li, who passed away in December 2020.

SUPPORTING INFORMATION

Details of the precursors of WS_2 and PVT growth parameters (Table 1), Preparation of suspended WS_2 on a TEM quantifoil grid for HAADF-STEM imaging (Figure S1), Terminology used for the wet transferred WS_2 sample on a TEM quantifoil grid (Table 2), Mass-spectrum acquired from the cluster source, which is demonstrating the mass resolution of the source (Figure S2), Linear relationship between the HAADF Intensity and number of WS_2 atomic layers(Figure S3), movie file: freestanding WS_2 monolayer under electron beam (Figure S4), molecular atomic models of 2H & 3R phase WS_2

(Figure S5), X-ray photo electron spectroscopy of as-grown WS_2 atomic layers (Figure S6, SI1), HAADF-STEM images of WS2-Pt_{147} hybrid (Figure S7). Simultaneous ADF and BF STEM images highlighting remnant carbon layer (Figure S8), Statistical analysis of Pt_{147} size selected nanoclusters (Figure S9, SI2), High resolution ADF STEM showing Pt_{147} cluster structure (Figure S10), Raman/Photoluminescence (PL) mapping of as-grown WS_2 (Figure S11), Details of the Lorentzian fitting parameters of 2_{LA}, E_{2g} and A_{1g} (Table 3 & Table 4), Comparative PL spectra of suspended WS_2 and WS_2-Pt_{147} nano clusters (Figure S12), analysis of real-time HAADF-STEM imaging of suspended WS_2-Pt_{147} (Figure S13), and a movie file: free-standing monolayer WS_2-Pt_{147} under ebeam.gif are provided here (Figure S14). This material is available free of charge via the Internet at http://pubs.acs.org.

REFERENCES:

1. Popok, V. N.; Barke, I.; Campbell, E. E. B.; Meiwes-Broer, K.-H. Cluster–Surface Interaction: From Soft Landing to Implantation. *Surf. Sci. Rep.* **2011**, *66*, 347-377.
2. Claridge, S. A.; Castleman, A. W.; Khanna, S. N.; Murray, C. B.; Sen, A.; Weiss, P. S. Cluster-Assembled Materials. *ACS Nano.* **2009**, *3*, 244-255.
3. Wang, B.; Yoon, B.; König, M.; Fukamori, Y.; Esch, F.; Heiz, U.; Landman, U. Size-Selected Monodisperse Nanoclusters on Supported Graphene: Bonding, Isomerism, and Mobility. *Nano Lett.* **2012**, *12*, 5907-5912.
4. Biroju, R. K.; Giri, P. K. Defect Enhanced Efficient Physical Functionalization of Graphene with Gold Nanoparticles Probed by Resonance Raman Spectroscopy. *J. Phys. Chem. C* **2014**, *118*, 13833-13843.
5. Plant, S. R.; Cao, L.; Yin, F.; Wang, Z. W.; Palmer, R. E. Size-Dependent Propagation of Au Nanoclusters through Few-Layer Graphene. *Nanoscale.* **2014**, *6*, 1258-1263.
6. Wang, S.; Sawada, H.; Han, X.; Zhou, S.; Li, S.; Guo, Z. X.; Kirkland, A. I.; Warner, J. H. Preferential Pt Nanocluster Seeding at Grain Boundary Dislocations in Polycrystalline Monolayer MoS_2. *ACS Nano.* **2018**, *12*, 5626-5636.
7. Bromann, K.; Félix, C.; Brune, H.; Harbich, W.; Monot, R.; Buttet, J.; Kern, K. Controlled Deposition of Size-Selected Silver Nanoclusters. *Science.* **1996**, *274*, 956.
8. Palmer, R. E.; Pratontep, S.; Boyen, H. G., Nanostructured Surfaces from Size-Selected Clusters. *Nat. Mater.* **2003**, *2*, 443-448.
9. Wang, S.; Sawada, H.; Chen, Q.; Han, G. G. D.; Allen, C.; Kirkland, A. I.; Warner, J. H. In Situ Atomic-Scale Studies of the Formation of Epitaxial Pt Nanocrystals on Monolayer Molybdenum Disulfide. *ACS Nano* **2017**, *11*, 9057-9067.
10. Zhang, Q.; Mei, L.; Cao, X.; Tang, Y.; and Zeng, Z., Intercalation and exfoliation chemistries of transition metal dichalcogenides. *J. Mater. Chem. A* ***2020****, 8, 15417-15444*.

11. Xu, C.; Wang, X.; Zhu, J. Graphene−Metal Particle Nanocomposites. *J. Phys. Chem. C* **2008**, *112*, 19841-19845.
12. Giovannetti, G.; Khomyakov, P. A.; Brocks, G.; Karpan, V. M.; van den Brink, J.; Kelly, P. J. Doping Graphene with Metal Contacts. *Phys. Rev. Lett.* **2008**, *101*, 026803.
13. Zan, R.; Bangert, U.; Ramasse, Q.; Novoselov, K. S. Metal−Graphene Interaction Studied Via Atomic Resolution Scanning Transmission Electron Microscopy. *Nano Lett.* **2011**, *11*, 1087-1092.
14. Zan, R.; Bangert, U.; Ramasse, Q.; Novoselov, K. S. Interaction of Metals with Suspended Graphene Observed by Transmission Electron Microscopy. *J. Phys. Chem. Lett.* **2012**, *3*, 953-958.
15. Li, S.; Lee, J. K.; Zhou, S.; Pasta, M.; Warner, J. H. Synthesis of Surface Grown Pt Nanoparticles on Edge-Enriched Mos2 Porous Thin Films for Enhancing Electrochemical Performance. *Chem. Mater.* **2019**, *31*, 387-397.
16. Xu, W,; Li, S.; Ryu, G. H.; Tang, P.; Pasta, M.; Warner, J. H. Single-Step Chemical Vapor Deposition Growth of Platinum Nanocrystal: Monolayer MoS2 Dendrite Hybrid Materials for Efficient Electrocatalysis. *Chem. Mater.* **2020**, *32*, 8243–8256.
17. Mei, L.; Gao, X.; Gao, Z.; Zhang, Q.; Yu, X.; Rogach, A. L.; and Zeng. Size-selective synthesis of platinum nanoparticles on transition-metal dichalcogenides for the hydrogen evolution reaction. *Chem. Commun*. **2021**, *57*, 2879-2882.
18. Strasser, P. Catalysts by Platonic design. *Science* **2015**, *349*, 379-380.
19. Hartl, K.; Nesselberger, M.; Mayrhofer, K. J. J.; Kunz, S.; Schweinberger, F. F.; Kwon, G.; Hanzlik, .; Heiz, U.; Arenz, M. Electrochemically induced nanocluster migration, *Electrochimica Acta* **2010**, *56*, 810-816.
20. Yoshida, K.; Bright, A.; Tanaka, N. Direct observation of the initial process of Ostwald ripening using spherical aberration-corrected transmission electron microscopy, *J. Electron Microsc.* **2012**, *61*, 0022-0744.
21. Cherevko, S.; Zeradjanin, A.R.; Topalov, A.A.; Kulyk, N.; Katsounaros, I. and Mayrhofer, K. J. J. Dissolution of Noble Metals during Oxygen Evolution in Acidic Media. *ChemCatChem* **2014**, *6*, 2219-2223.
22. Dubau, L.; Castanheira, L.; Berthomé, G.; Maillard, F. An identical-location transmission electron microscopy study on the degradation of Pt/C nanoparticles under oxidizing, reducing and neutral atmosphere. *Electrochim. Acta* **2013**, *110*, 273-281.
23. Kunz, S.; Hartl, K.; Nesselberger, M.; Schweinberger, F.F.; Kwon, G.; Hanzlik, M.; Mayrhofer, K.J.J.; Heiza, Ueli.; Arenz, M. Size-selected clusters as heterogeneous model catalysts under applied reaction conditions. *Phys. Chem. Chem. Phys.* **2010**, *12*, 10288-10291.
24. Ustarroz, J.; Ornelas, I.M.; Zhang, G.; Perry, D.; Kang, M.; Bentley, C.L.; Walker, M.; and Unwin, P.R. Mobility and Poisoning of Mass-Selected Platinum Nanoclusters during the Oxygen Reduction Reaction. ACS Catal. **2018**, *8*, 6775-6790.
25. Wettergren, K.; Schweinberger, F.F.; Deiana, D.; Ridge, C.J.; Crampton, A.S.; Rötzer, M.D.; Hansen, T.W.; Zhdanov, V.P.; Heiz, U.; and Langhammer, C. High Sintering Resistance of Size-Selected Platinum Cluster Catalysts by Suppressed Ostwald Ripening. Nano Lett. **2014** *14*, 10, 5803-5809.
26. Arán-Ais, R.M.; Vidal-Iglesias, F.J.; Solla-Gullón, J.; Herrero, E.; and Feliu, J.M. Electrochemical Characterization of Clean Shape-Controlled Pt Nanoparticles Prepared in Presence of Oleylamine/Oleic Acid. *Electroanalysis* **2015**, *27*, 945-956.

27. Lambie, S. G.; Weal, G. R.; Blackmore, C.E.; Palmer, R.E.; and Garden, A.L. Contrasting motif preferences of platinum and gold nanoclusters between 55 and 309 atoms Nanoscale Adv. **2019**, 1, 2416-2425.
28. Baletto, F.; Ferrando, R.; Fortunelli, A.; Montalenti, C. Mottet Crossover among structural motifs in transition and noble-metal clusters. The J. Chem. Phys. **2002**, *116*, 3856-3863.
29. Xia, Y.; Nelli, D.; Ferrando, R.; Yuan, J.; and Li, Z. Y. Shape control of size-selected naked platinum nanocrystals. *Nat Commun* **2021**, *12*, 3019.
30. Martin, T.P. Shells of atoms. *Phys. Rep.* **1996,** *273*, 4, 199-241.
31. Hu, K-J.; Plant, S.R.; Ellis, P.R.; Brown, C.M.; Bishop, P.T.; and Palmer, R.E. Atomic Resolution Observation of a Size-Dependent Change in the Ripening Modes of Mass-Selected Au Nanoclusters Involved in CO Oxidation. *J. Am. Chem. Soc.* **2015**, *137*, 48, 15161–15168.
32. Foster, D.M.; Ferrando, R.; Palmer, R. E. Experimental determination of the energy difference between competing isomers of deposited, size-selected gold nanoclusters. *Nat. Commun*. **2018**, *9*, 1323.
33. Plant, S. R.; Cao, L.; and Palmer, R.E. Atomic Structure Control of Size-Selected Gold Nanoclusters during Formation. **2014**, *J. Am. Chem. Soc. 136*, 21, 7559–7562
34. Li, Z.; Young, N.; Di Vece, M.; Palomba, S.; Palmer, R. E.; Bleloch, A. L.; Curley, B. C.; Johnston, R. L.; Jiang, J.; Yuan, J. Three-dimensional atomic-scale structure of size-selected gold nanoclusters. **2008,** *Nature 451*, 46–48.
35. Goldby, I. M.; Issendorff, B. V.; Kuipers, L.; Palmer, R. E. Gas Condensation Source for Production and Deposition of Size-Selected Metal Clusters. *Rev. Sci. Instrum.* **1997**, *68*, 3327-3334.
36. Pratontep, S.; Carroll, S. J.; Xirouchaki, C.; Streun, M.; Palmer, R. E. Size-Selected Cluster Beam Source Based on Radio Frequency Magnetron Plasma Sputtering and Gas Condensation. *Rev. Sci. Instrum.* **2005**, *76*, 045103.
37. Issendorff, B. V.; Palmer, R. E. A New High Transmission Infinite Range Mass Selector for Cluster and Nanoparticle Beams. *Rev. Sci. Instrum.* **1999**, *70*, 4497-4501.
38. Wang, Z. W.; Toikkanen, O.; Yin, F.; Li, Z. Y.; Quinn, B. M.; Palmer, R. E. Counting the Atoms in Supported, Monolayer-Protected Gold Clusters. *J. Am. Chem. Soc.* **2010**, *132*, 2854-2855.
39. Jian, N.; Stapelfeldt, C.; Hu, K.-J.; Fröba, M.; Palmer, R. E. Hybrid Atomic Structure of the Schmid Cluster $Au_{55}(PPh_3)_{12}Cl_6$ Resolved by Aberration-Corrected Stem. *Nanoscale* **2015**, *7*, 885-888.
40. Nellist, P. D.; Pennycook, S. J.; , Hawkes, P. W. The Principles and Interpretation of Annular Dark-Field Z-Contrast Imaging. In *Adv. Imaging Electron Phys.* **2000**, *113*, 147-203.
41. Treacy, M. M. J.; Howie, A.; Wilson, C. J., Z Contrast of Platinum and Palladium Catalysts. *Philos. Mag. A* **1978**, *38*, 569-585.
42. Crewe, A. V.; Wall, J.; Langmore, J. Visibility of Single Atoms. *Science.* **1970**, *168*, 1338-1340.
43. Wang, S.; Robertson, A.; Warner, J. H., Atomic structure of defects and dopants in 2D layered transition metal dichalcogenides. Chem. Soc. Rev. **2018**, *47*, 6764
44. Zhou, Z.; Li, B.; Shen, C.; Wu, D.; Fan, H.; Zhao, J.; Li, H.; Zeng, Z.; Luo, Z.; Ma, L.; Tan, C. Metallic 1T Phase Enabling MoS_2 Nanodots as an Efficient Agent for Photoacoustic Imaging Guided Photothermal Therapy in the Near-Infrared-II Window. *Small **2020**, 16, 2004173*.

45. Weston, A., Zou, Y., Enaldiev, V. et al. Atomic reconstruction in twisted bilayers of transition metal dichalcogenides. Nat. Nanotechnol. 15, 592–597 (2020).
46. Xia, Y.; Harrison, P.; Ornelas, I.M.; Wang, H.L.; Li, Z.Y. HAADF-STEM image analysis for size-selected platinum nanoclusters. J. Microsc. **2020,** *279*, 229–233.
47. McCreary, K. M.; Hanbicki, A. T.; Singh, S.; Kawakami, R. K.; Jernigan, G. G.; Ishigami, M.; Ng, A.; Brintlinger, T. H.; Stroud, R. M.; Jonker, B. T. The Effect of Preparation Conditions on Raman and Photoluminescence of Monolayer WS_2. *Sci. Rep.* **2016**, *6*, 35154.
48. Berkdemir, A; Gutiérrez, H.R.; Botello-Méndez, A.R.; Perea-López, N.; Elías, A.L.; Chia, C.; Wang, B.; Crespi, V. H.; López-Urías, F.; Charlier, J. C.; Terrones, H.; Terrones, M. Identification of Individual and Few Layers of WS_2 Using Raman Spectroscopy. *Sci. Rep.* **2013**, 3, 1755.
49. Cong, C., Shang, J., Wu, X., Cao, B., Peimyoo, N., Qiu, C., Sun, L. and Yu, T. Synthesis and Optical Properties of Large-Area Single-Crystalline 2D Semiconductor WS_2 Monolayer from Chemical Vapor Deposition. *Adv. Opt. Mater.* **2014**, *2*, 131-136. doi:10.1002/adom.201300428
50. Biroju, R.K., Pal, S., Sharma, R., Giri, P. K., Narayanan, T. N. Stacking Sequence Dependent Photo-Electrocatalytic Performance of CVD Grown MoS_2/Graphene Van Der Waals Solids. Nanotechnology. **2017**, *28*, 085101.
51. Ding, Y.; Zheng, W.; Jin, M.; Zhu, Y.; Zhu, R.; Lin, Z.; Huang, F. Raman tensor of layered MoS2. Opt. Lett. **2020**, *45*, 1313-1316.
52. Ding, Y.; Zheng, W.; Lin, Z.; Zhu, R.; Jin, M.; Zhu, Y.; Huang, F. Raman tensor of layered WS_2. *Sci. China Mater*. **2020,** *63*, 1848–1854
53. Sasaki, S.; Kobayashi, Y.; Liu, Z.; Suenaga, K.; Ma. Y. Growth and optical properties of Nb-doped WS_2 monolayers. *Appl. Phys. Express* **2016,** *9*, 071201.
54. Pham, V.P. and Yeom, G.Y. Recent Advances in Doping of Molybdenum Disulfide: Industrial Applications and Future Prospects. *Adv. Mater.* **2016**, *28*: 9024-9059.

Graphic for manuscript

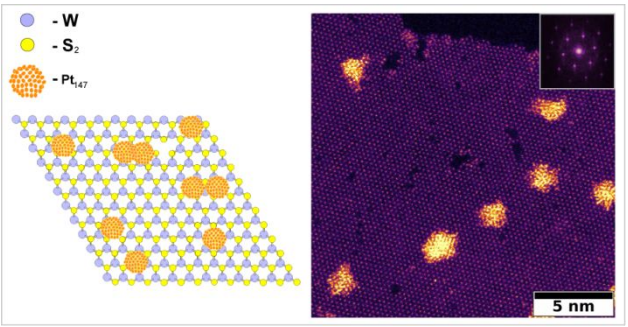

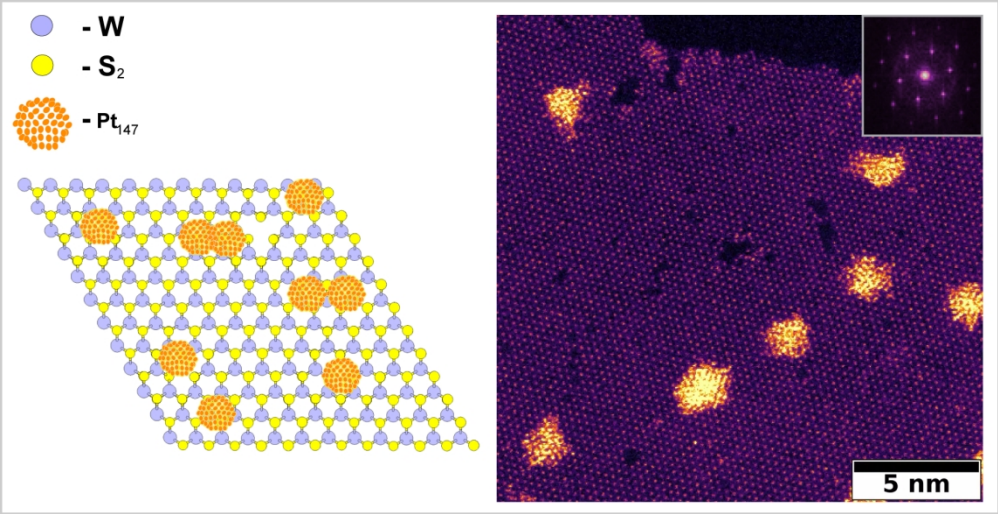

WS_2-Pt_{147} Hybrid Nanostructured 2D Materials